Chemical Engineering Journal 462 (2023) 142192

Contents lists available at ScienceDirect

Chemical Engineering Journal

journal homepage: www.elsevier.com/locate/cej

ROS filter coating scaffold protects 3D mesenchymal stem cell spheroids for dual-phase treatment of spinal cord injury

Jian Cao [a,1], Jiahe Wu [a,1], Jiafu Mu [a], Lingmin Lin [f], Xunqi Zhang [a], Tianchen Huang [a], Teng Ma [a], Manning Zhu [a], Xiaoyang Dai [g], Xuhua Wang [f], Shiqing Feng [d,e,*], Jian-Qing Gao [a,b,c,*]

[a] College of Pharmaceutical Sciences, Zhejiang University, Hangzhou 310058, China
[b] Dr. Li Dak Sum & Yip Yio Chin Center for Stem Cell and Regenerative Medicine, Zhejiang University, Hangzhou 310058, China
[c] Jinhua Institute of Zhejiang University, Jinhua 321002, China
[d] Department of Orthopaedics, Tianjin Medical University General Hospital, Tianjin Key Laboratory of Spine and Spinal Cord, Tianjin 300052, China
[e] The Second Hospital of Shandong University, Cheeloo College of Medicine, Shandong University, Jinan 250012, China
[f] Department of Neurobiology and Department of Rehabilitation Medicine, The First Affiliated Hospital, Zhejiang University School of Medicine, Hangzhou 310003, China
[g] Center for Drug Safety Evaluation and Research, College of Pharmaceutical Sciences, Zhejiang University, Hangzhou 310058, China

ARTICLE INFO

Keywords:
Spinal cord injury
ROS scavenging
Mesenchymal stem cell spheroid
Functional scaffold
Tissue engineering

ABSTRACT

Implanting mesenchymal stem cells (MSCs) has offered a great promise in spinal cord injury (SCI) repair. However, the harsh environment accompanied with excessive ROS following SCI seriously threatens MSC survival and compromises its efficacy. Additionally, the intricate pathology distinguished as the acute phase and chronic phase makes MSC therapeutics alone difficult to alleviate severe inflammation and promote functional recovery simultaneously. Despite scaffold systems for local stem cell delivery being extensively explored, dual-phase management for SCI using one protective scaffold system has rarely been reported. Herein, a composite scaffold system (RF-pGel-MS), which consisted of an outer ROS filter (RF) and an inner porous GelMA hydrogel (pGel) harbored with MSC spheroids (MSs), was designed for SCI repair. Specifically, RF rapidly scavenged ROS, protecting the MS from peroxidation damage in the acute phase. MS constructed via 3D culture of MSCs presented enhanced paracrine effects, which remarkably facilitated neuron repair and functional recovery in the chronic phase. The dual-phase therapeutic efficacy of RF-pGel-MS led to significant locomotor and electrophysiology recovery in the SCI rats. Hence, the currently proposed strategy using RF-pGel-MS is efficient for ROS scavenging and boosting the stem cell therapeutics, which is insightful for the SCI treatment.

1. Introduction

Spinal cord injury (SCI) is a severe disease occurred in central nervous system (CNS), which dramatically impairs neuron conduction to and from brain, leading to paralysis, organ dysfunction and even death [1,2]. The pathological process of SCI is intricate and exhibits distinctly different features in the acute phase and chronic phase [3]. It has a consensus that the secondary injury in the acute phase and limited neuronal regeneration in the chronic phase are the major obstacles to be overcome. Consequently, SCI rehabilitation requires a multipotent therapeutic strategy.

Growing research over the past decades suggests that MSC therapy holds a considerable promise in SCI repair [4]. Locally implanted MSCs secret a variety of versatile paracrine effectors that have neurotrophic, anti-inflammatory and angiogenic effect for comprehensive regulation after SCI. However, the therapeutic effect of MSCs is severely hindered by their low survival rate and activity in the inflammatory acute phase [5,6]. Although there are substantial studies about scaffold systems for local stem cell delivery since they can serve as an extracellular matrix (ECM) for injured tissue and a depot for MSCs simultaneously, a scaffold system with dual-phase treatment capacity is urgently needed.

Specifically, the overproduced ROS in acute phase has been proved one of the pivotal signaling molecules that mediate secondary injury following SCI. Excessive ROS are extensively involved in the oxidative

* Corresponding authors at: Department of Orthopaedics, Tianjin Medical University General Hospital, Tianjin Key Laboratory of Spine and Spinal Cord, Tianjin 300052, China (S. Feng) and College of Pharmaceutical Science, Zhejiang University, Hangzhou 310058, China (J.-Q. Gao).
E-mail addresses: sqfeng@tmu.edu.cn (S. Feng), gaojianqing@zju.edu.cn (J.-Q. Gao).
[1] These authors contributed equally to this work.

https://doi.org/10.1016/j.cej.2023.142192
Received 26 November 2022; Received in revised form 21 February 2023; Accepted 25 February 2023
Available online 2 March 2023

reactions with lipids and proteins [7,8], which produce highly cytotoxic 4-hydroxynonenal (4-HNE) and 2-propenal, leading to ionic imbalance and protein damage. Ultimately, the uncontrolled oxidative process causes mitochondrial dysfunction, metabolic failure and DNA damage, resulting in massive death of endogenous cells and implanted stem cells [9,10]. In light of these findings, we hypothesize that integrating a ROS scavenging scaffold with stem cell implantation would effectively reduce the secondary injury, potentiate the therapeutic activity of MSCs, and achieve dual-phase management at the meantime.

Inspired by the previous studies of introducing ROS-cleavable chemical groups (e.g., phenylboronic acid and thioketal) to fabricate ROS-responsive or ROS-scavenging scaffolds [11,12], we herein construct a ROS filter (RF) via the crosslink of polyvinyl alcohol (PVA) and phenylboronic acid-based, ROS-responsive linker, N^1-(4-boronobenzyl)-N^3-(4-boronophenyl)-N^1,N^1,N^3,N^3-tetramethylpropane-1,3-diaminium (TPA). RF is then coated around the porous GelMA scaffold (pGel) to form a double-layered scaffold (RF-pGel). In order to further lessen the susceptibility, the MSCs are 3D cultured and assembled into MSC spheroids (MSs), which are loaded into the inner layer of RF-pGel (Fig. 1A). Following implanting into lesions of SCI, the outer RF rapidly scavenges ROS and degrades simultaneously, thus mitigates the expansion of secondary injury and protects the inner MS from peroxidative damage in the acute phase. Compared with 2D MSCs, MSs with 3D structure mimic the *in vivo* condition of MSCs, and exhibit more intercellular communications and enhanced paracrine effects, which are beneficial for promoting neural repair and regeneration in the chronic phase (Fig. 1B). Consequently, double layer-structured RF-pGel-MS with ROS elimination and strengthened regulation capability of MSC holds a great promise for the dual-phase treatment of difficult-to-heal SCI.

2. Results

2.1. Construction and characterization of RF-pGel-MS

RF-pGel-MS was composed of an outer RF, an inner pGel and encapsulated MSs. To be specific, the ROS-responsive linker, TPA, was successfully synthesized (Fig. S1) and the structure was confirmed by proton nuclear magnetic resonance (^{1}H NMR) (Fig. S2). RF was formed by the reactions between phenylboronic acid on TPA and dihydroxyl group on PVA (Fig. S3). The crosslink process was quickly completed in seconds via simple mixing (Fig. 2A). pGel was formed by the UV curing of porous GelMA solution. MS was loaded in pGel by mixing with GelMA solution and UV crosslink. Finally, RF was coated around pGel or pGel-MS to formed RF-pGel or RF-pGel-MS (Fig. 2B). The thickness of outer RF was controlled to avoid occupying the volume of pGel, that is, the living space of MS. The two sides of pGel-MS were kept uncovered to guarantee the nutrition exchange of MS (Fig. 2B). Scanning electron microscope image revealed the dense network structure of RF with abundant pores (Fig. 2C). Compared with RF, pGel showed a similar porous network structure, but with larger pores (Fig. 2D). Rheological test of RF and pGel showed $G' > G''$ (Fig. S4), proving the viscoelastic solid nature of them. The elastic module of pGel was similar to the natural CNS tissue (0.1 ~ 16 kPa) [13]. MS was fabricated by 3D culture of MSCs. The tight cellular arrangement of MSCs were observed on the

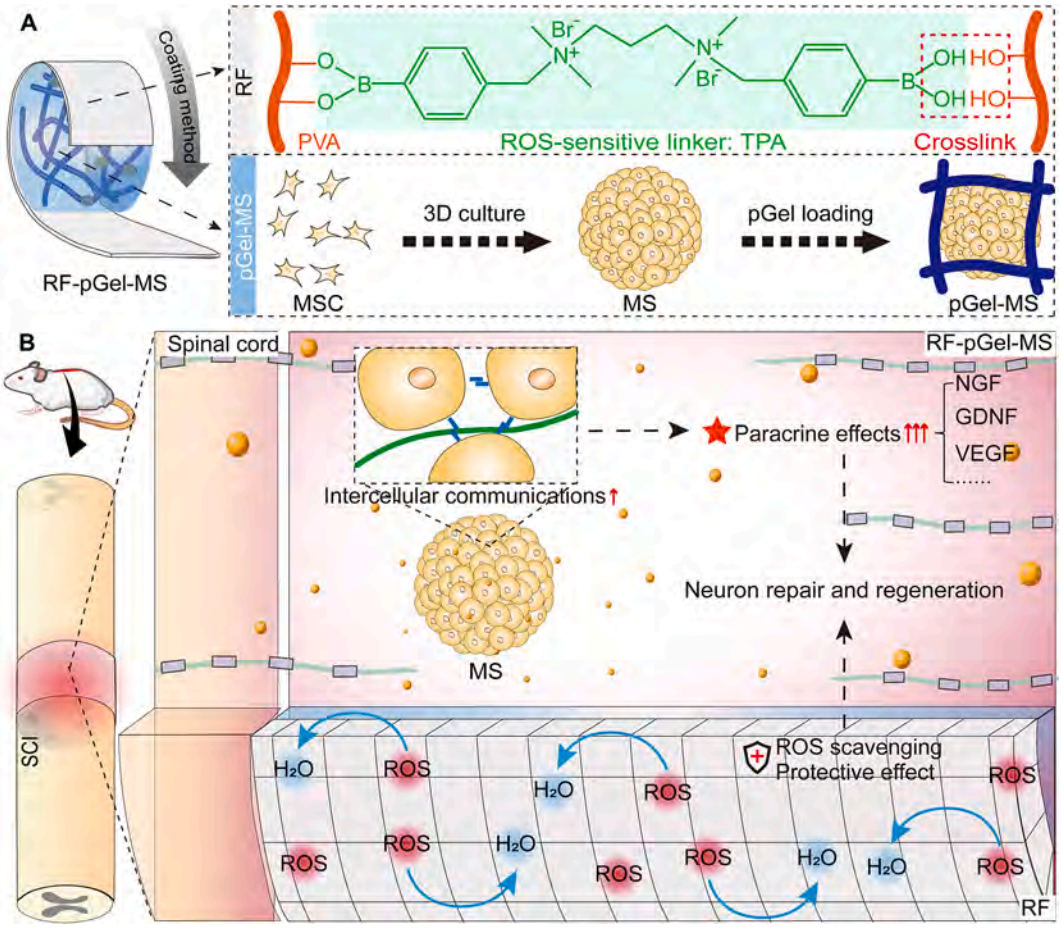

Fig. 1. Schematic illustration for the construction of RF-pGel-MS and its therapeutic strategies for SCI repair. (A) RF was formed via the crosslink of PVA and ROS-responsive linker, TPA. MS was constructed by 3D-culture of MSCs and then encapsulated in pGel by ultraviolet (UV) curing. Finally, RF was coated around the pGel-MS to form double-layered RF-pGel-MS. (B) RF-pGel-MS was implanted in lesion of SCI for scavenging over-produced ROS, protecting MS from peroxidative injury, and promoting tissue regeneration via enhanced paracrine effect of MS.

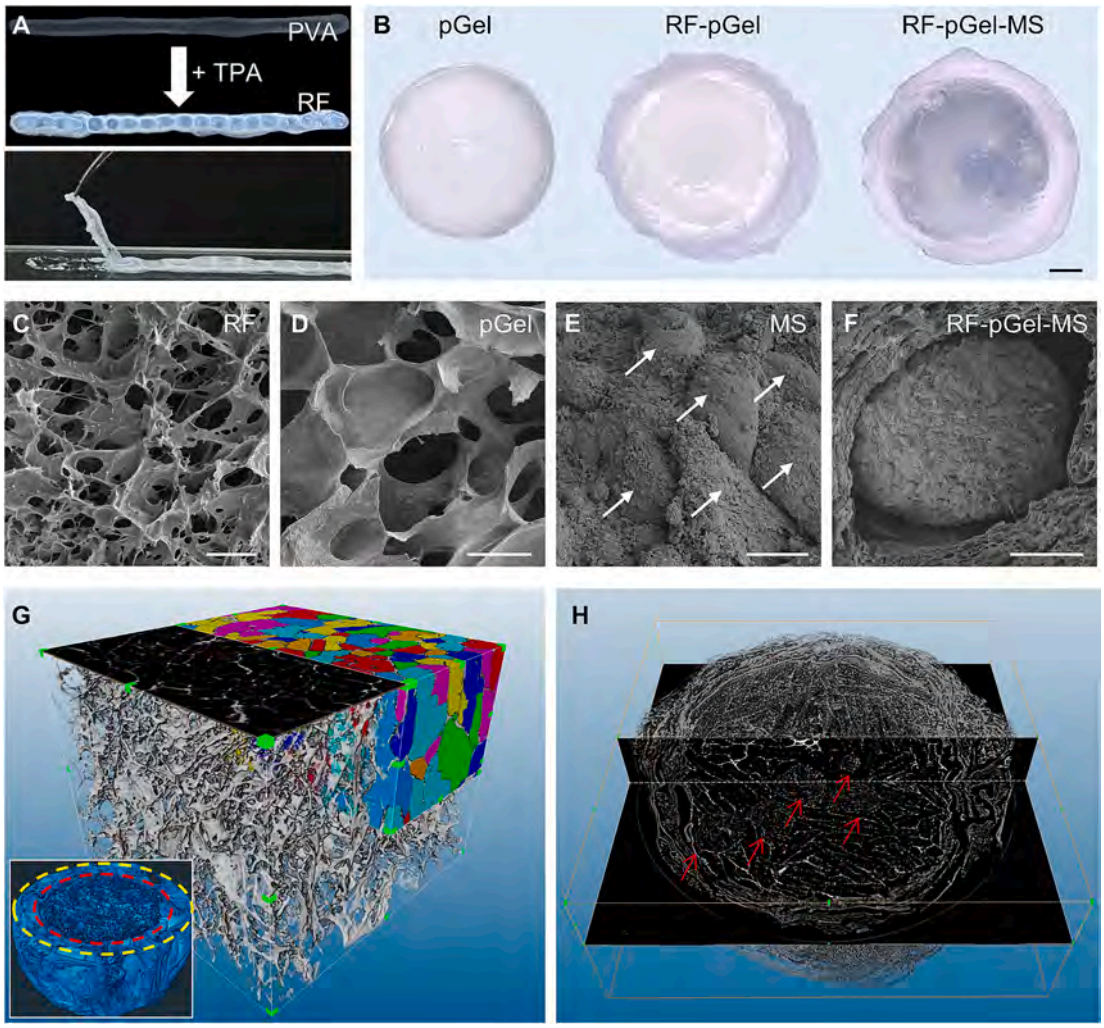

Fig. 2. Characterization of RF-pGel-MS. (A) RF was formed by the mixing of PVA and TPA. (B) Photographs of pGel, RF-pGel and RF-pGel-MS. Scale bar: 500 μm. (C and D) The structures of RF (scale bar: 10 μm) and pGel (scale bar: 100 μm) detected by scanning electron microscope. (E) The surface structure of MS (scale bar: 10 μm). White arrows indicated MSCs. (F) MS was encapsulated in pGel and immobilized via steric hindrance. Scale bar: 100 μm. (G) RF-pGel was scanned by microCT and reconstructed into 3D images. The pore distribution of pGel was analyzed using Avizo software. (H) RF-pGel-MS was scanned by microCT to detect the MS distribution. Red arrows indicated the MSs. (For interpretation of the references to color in this figure legend, the reader is referred to the web version of this article.)

surface of MS (Fig. 2E). Due to the micron size of MS, MS can be easily encapsulated in pGel and immobilized via steric hindrance (Fig. 2F).

The whole structure of RF-pGel-MS was scanned by high-resolution microCT, and the reconstruction image clearly showed a double layer structure (picture embedded in Fig. 2G). Then the inner pGel was selectively analyzed using Avizo software as it had a direct impact on MS vitality. The reconstruction image containing 2D and 3D information and pore distributions of pGel was shown in Fig. 2G. The plates with different colors in image represented pores with different sizes. Based on these data, volume fraction, pore area and pore volume were calculated. It presented the uniform pore distribution at each layer while inhomogeneous pore size of pGel. The average pore area and volume were 138430 μm^2 and 3312148 μm^3, respectively (Fig. S5). The reconstruction image combined with video (Vedio S1) clearly demonstrated MS randomly distributed in RF-pGel-MS as red arrows indicated (Fig. 2H).

2.2. Enhanced paracrine and neurotrophic effects of MS

Due to the elevated cell–cell contacts and cell-extracellular matrix interactions, MSCs easily self-assembled and formed MS after seeding in the non-adhesive plate (Fig. S6). By altering the cell number, the diameter of MS can be variably changed from 0.5 to 1 mm (Fig. 3A and 3B). MSs were encapsulated in pGel via UV curing and still kept spheroid structure after 7-day culture. It is notable that several tentacle-like structures on the surface of MS extended to pGel, which may enhance adhesion of MS on pGel (Fig. 3C).

Paracrine effect is one of the key mechanisms of MSC therapeutics. In SCI, increasing evidence contributes various MSC-induced functional improvements to its secretion ability [8]. To verified the enhanced paracrine effects of MS, nerve growth factor (NGF), glial-derived neurotrophic factor (GDNF) and vascular endothelial growth factor (VEGF) in culture medium of MSs were measured using ELISA kits. Compared with 2D MSCs, 3D MSs of various sizes (MS1, MS2, MS3, total cell number: 1.8×10^5) expressed much higher GDNF, NGF and VEGF. Though there was no significance, MS2 and MS3 secreted relatively more factors than MS1. It's interesting to note that VEGF expression levels in both MSCs and MSs are higher than NGF and GDNF, which is probably due to the umbilical cord source of MSCs (Fig. 3D-3F).

PC12 cells, a cell line that, when stimulated by NGF, can develop into ganglion-like cells, which were widely used in neuron studies [14]. To test the neurotrophic potential of MS, PC12 cells were co-cultured with pGel-MS or pGel-MSC. And Cell differentiation was monitored every day. On day 3, no cells differentiated in control group without NGF. While a substantial increase in differentiation was found when co-

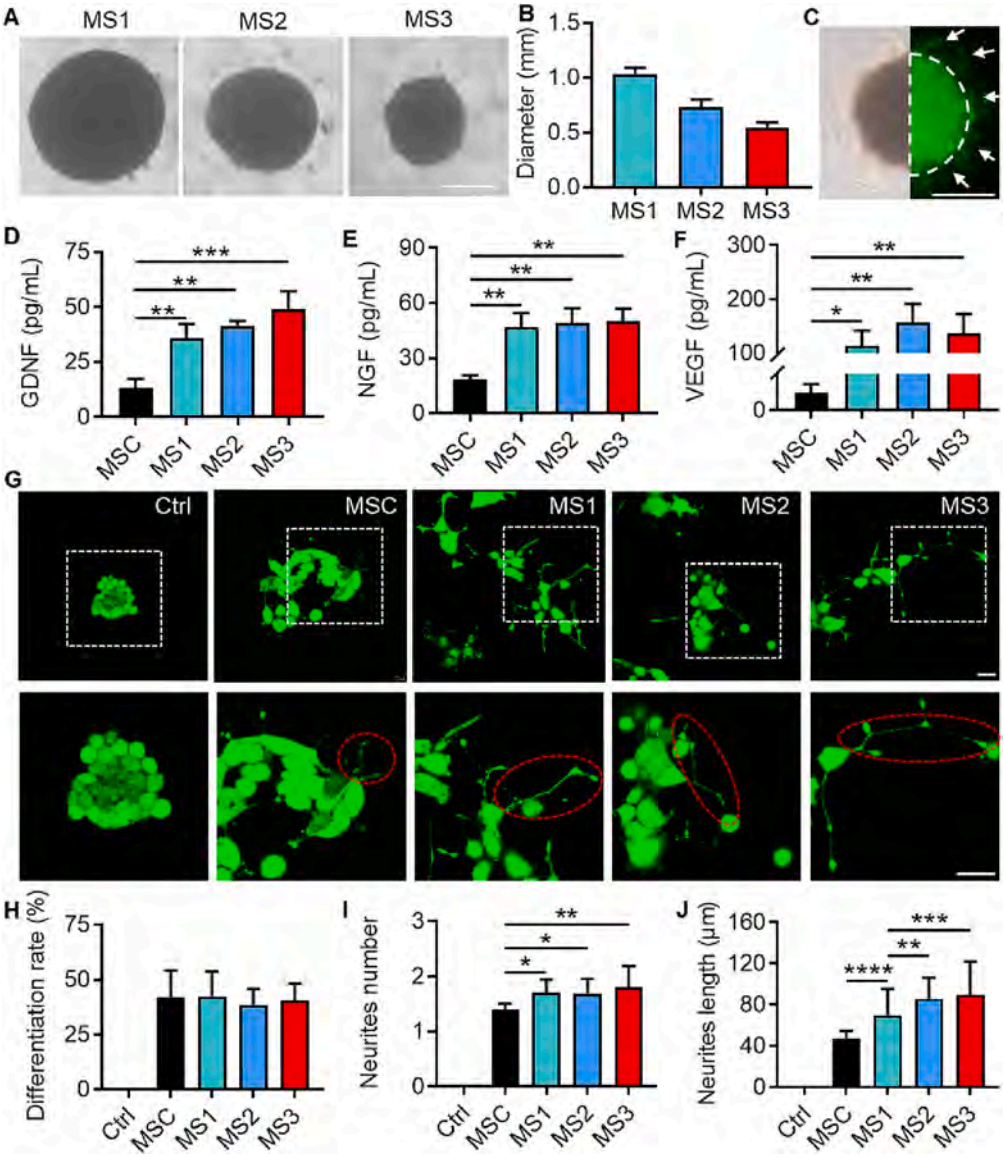

Fig. 3. Characterization of MS and its paracrine and neurotrophic effect. (A) MSs consisted of different numbers of MSCs (scale bar: 500 μm) and (B) its corresponding sizes (n = 3). (C) Morphology of MS encapsulated in pGel on day 7. White arrows indicated the tentacle-like structures on the surface and semicircle indicated the spheric boundary of MS. Scale bar: 500 μm. (D ~ F) Secretion levels of GDNF (D, n = 3), NGF (E, n = 3) and VEGF (F, n = 3) by MSCs and MS1, MS2, MS3 in culture medium. (G) Differentiation of PC12 cells after 3-day co-culture with MSCs, MS1, MS2 or MS3. The white square was the representative differentiated cells and the red oval was the extended neurites of cells in each group. Scale bar: 25 μm. (H-J) Quantitative analysis of differentiation rate (H, n = 4 × 3), average neurites number per cell (I, n = 4 × 3) and average neurites length in each group (J, n = 4 × 10). The data was shown as mean ± SD and analyzed by one-way ANOVA with multiple comparisons test. *P < 0.05, **P < 0.01, ***P < 0.001 and ****P < 0.0001. (For interpretation of the references to color in this figure legend, the reader is referred to the web version of this article.)

culturing with MSCs or MS (Fig. 3G). No significance in the differentiation rate of PC12 cells was found between pGel-MSCs and pGel-MS groups (Fig. 3H), which indicated that even a small amount of NGF already enabled PC12 cell differentiation. But the enhanced paracrine effect, that is, more NGF secretion derived from MS, resulted in more neurites number and longer neurites length of PC12 cells compared with MSCs. Meanwhile, MS2 and MS3 have a more significant improvement in neurites growth and elongation than MS1 (Fig. 3I and 3J). The result was in line with the result of the MS secretion test and proved the great neurotrophic effect of MS.

2.3. *Protective effect of RF on PC12 cells and MS*

ROS scavenging is vital for alleviating neural tissue damage and promoting the survival of implanted MS. After immersing in H_2O_2 solution, RF rapidly scavenged approximate 80% of H_2O_2 in 8 h (Fig. 4A) and transferred it into H_2O and O_2 (Fig. 4B). Moreover, RF gradually degraded in H_2O_2 solution within 6 d while remained intact in PBS solution, which posed a ROS-responsive degradation behavior (Fig. S7). The *in vivo* degradation also indicated that the outer RF had a rapid degradation and was completely degraded within 7 d, leaving transparent pGel-MS in spinal cord. Then the inner pGel was gradually degraded within 28 d and replaced by newly growing tissue (Fig. S8). The CCK-8 test showed that RF itself had no obvious cytotoxicity to PC12 cells (Fig. 4C). And the low cytotoxicity of RF, pGel, RF-pGel to both PC12 cells and MSCs ensured the safety of scaffold implantation (Fig. S9). To test the protective effect of RF on neuron, peroxidation injury was induced on PC12 cells using H_2O_2. The stimulation of H_2O_2 caused approximately 40% of cell death. Due to the rapid ROS scavenging ability, the addition of RFs containing various concentrations of TPA all dramatically improved the survival rate of PC12 cells (Fig. 4D). Furthermore, the intracellular ROS levels of PC12 cells with aforementioned treatments were detected by a fluorescent ROS probe, DCFH-DA. After H_2O_2 stimulation, the relative fluorescent intensity of cells was twice as high as that in the control group, whereas RF significantly decreased ROS level, which explained the improved cell survival rate in this group (Fig. 4E and S10).

Then the protective effect of RF on MS was also tested using live/dead assay and scanned by confocal microscope. The scanning depth was only about 200 μm because of the limited transmission of laser and optical opacity of MS. However, the obtained results have already reflected the survival conditions of superficial MSCs on MS. The reconstruction images showed that H_2O_2 induced a lot of red signals on MS, which means massive cell death. And the coating of RF on pGel-MS

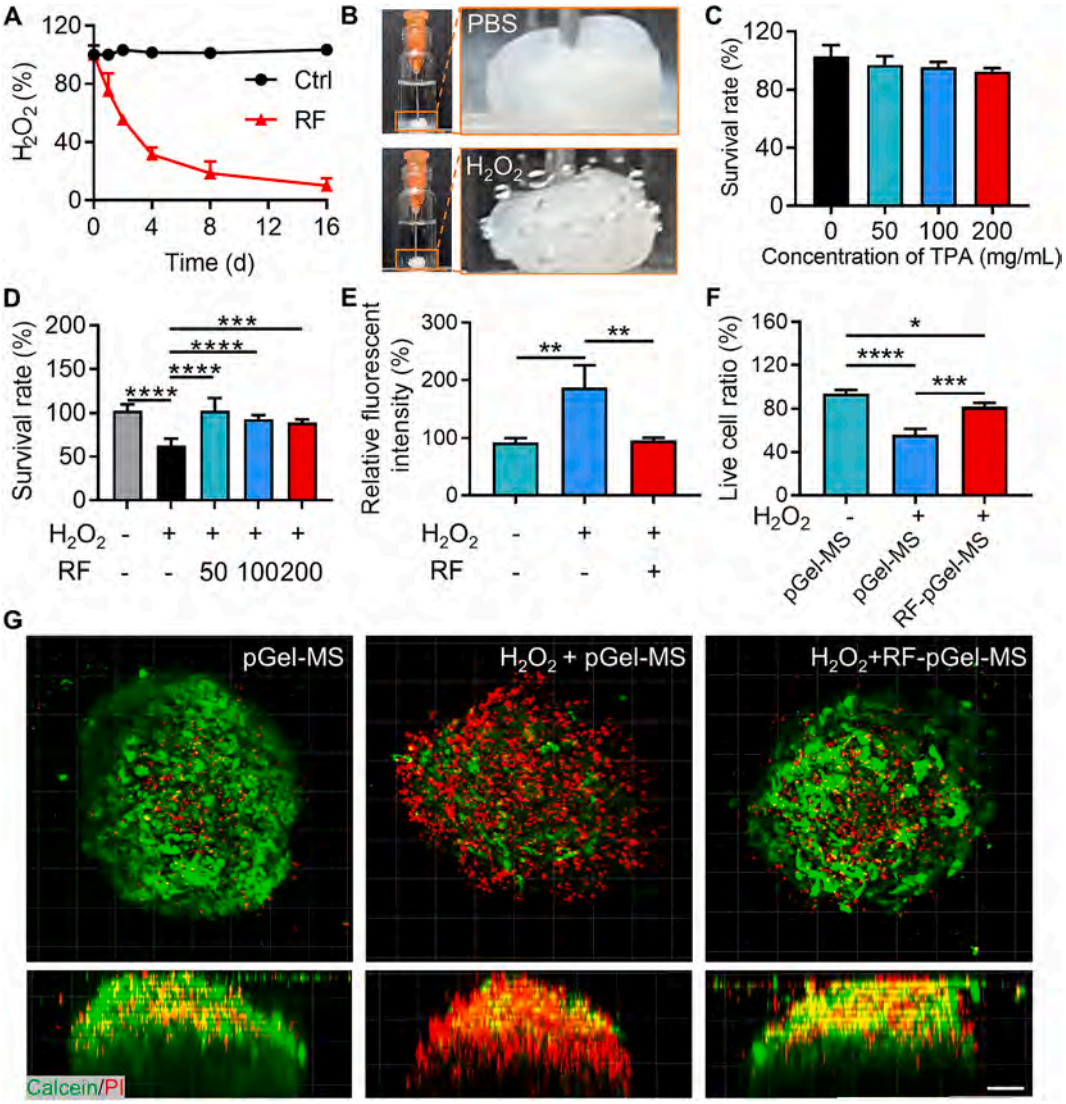

Fig. 4. ROS scavenging capacity of RF and its protective effect against peroxidative injury. (A) The concentrations of H_2O_2 solution incubated with or without RF at 0, 1, 2, 4, 8, 16 h, respectively (n = 3). (B) The oxygen generation of RF in PBS or H_2O_2 solution. (C) Cytotoxicities of RFs containing various concentrations of TPA in PC12 cells (n = 3). (D) The survival rate of H_2O_2-stimulated PC12 cells cultured with RFs containing various concentrations of TPA (n = 3). (E) Average intracellular ROS level of H_2O_2-stimulated PC12 cells cultured with or without RF (n = 3). (F, G) Live/dead condition of MSs in pGel-MS in H_2O_2 solution with or without the protection of RF and corresponding semi-quantitative analysis (n = 3). Scale bar: 100 μm. The data was shown as mean ± SD and analyzed by one-way ANOVA with multiple comparisons test. *P < 0.05, **P < 0.01, ***P < 0.001 and ****P < 0.0001.

significantly reduced cell death to a low degree (Fig. 4F and 4G). In a long-term experiment, massive cell death was caused by continuous H_2O_2 stimulation for 5 days, resulted in the collapse of MS structure in pGel-MS. Despite little dead cell existed around, MS in RF-pGel-MS still maintained spheroid structure (Fig. S11). Therefore, RF-pGel-MS had a great ability to protect the neuron and MS from peroxidative damage.

2.4. Anti-peroxidative effect of RF-pGel-MS in the acute phase

Since the overproduction of ROS mainly occurs in the acute phase, the anti-peroxidative effect of RF-pGel-MS was detected on rats on day 4 after SCI. A lot of signals of lipid peroxidation marker 4-hydroxynonenal (4-HNE) (Fig. 5A) and the DNA peroxidation marker 8-hydroxy-2′-deoxyguanosine (8-OHdG) (Fig. 5B) widely dispersed in the lesion of spinal cord in both SCI and pGel-MS groups. And RF-pGel-MS implantation effectively reduced their distributions and intensities (Fig. 5C). Interestingly, complete morphology of MS was observed in both pGel-MS and RF-pGel-MS groups as indicated by GFP signals (Fig. 5D). However, more numbers of MSs were found in tissues of RF-pGel-MS than pGel-MS group. Although the vitality of MS is yet unknown, MS in RF-pGel-MS seemed healthier than that in pGel-MS based on their morphologies (Fig. 5E). To figure out the underlying mechanism of anti-peroxidative effect, Nrf2/HO-1 expression in spinal cord tissue were determined by Western Blot. (Fig. 5F). Nrf2/HO-1 pathway is key signaling pathway that regulates endogenous oxidative stress. Once excessive ROS produced, the imbalance of redox would result in the activation of Nrf2/HO-1 pathway for anti-oxidation [15]. In contrast to normal tissue, a slight increase of Nrf2 and HO-1 expressions in SCI group was observed, which may be related to the stress response to the intense stimulus of SCI. pGel-MS implantation can promote the expression of both Nrf2 and HO-1, which is higher than that in SCI group. And this promotion effect was further enhanced in RF-pGel-MS group (Fig. 5G and 5H). Together, RF-pGel-MS effectively alleviated the peroxidative damage and protected MS *in vivo*.

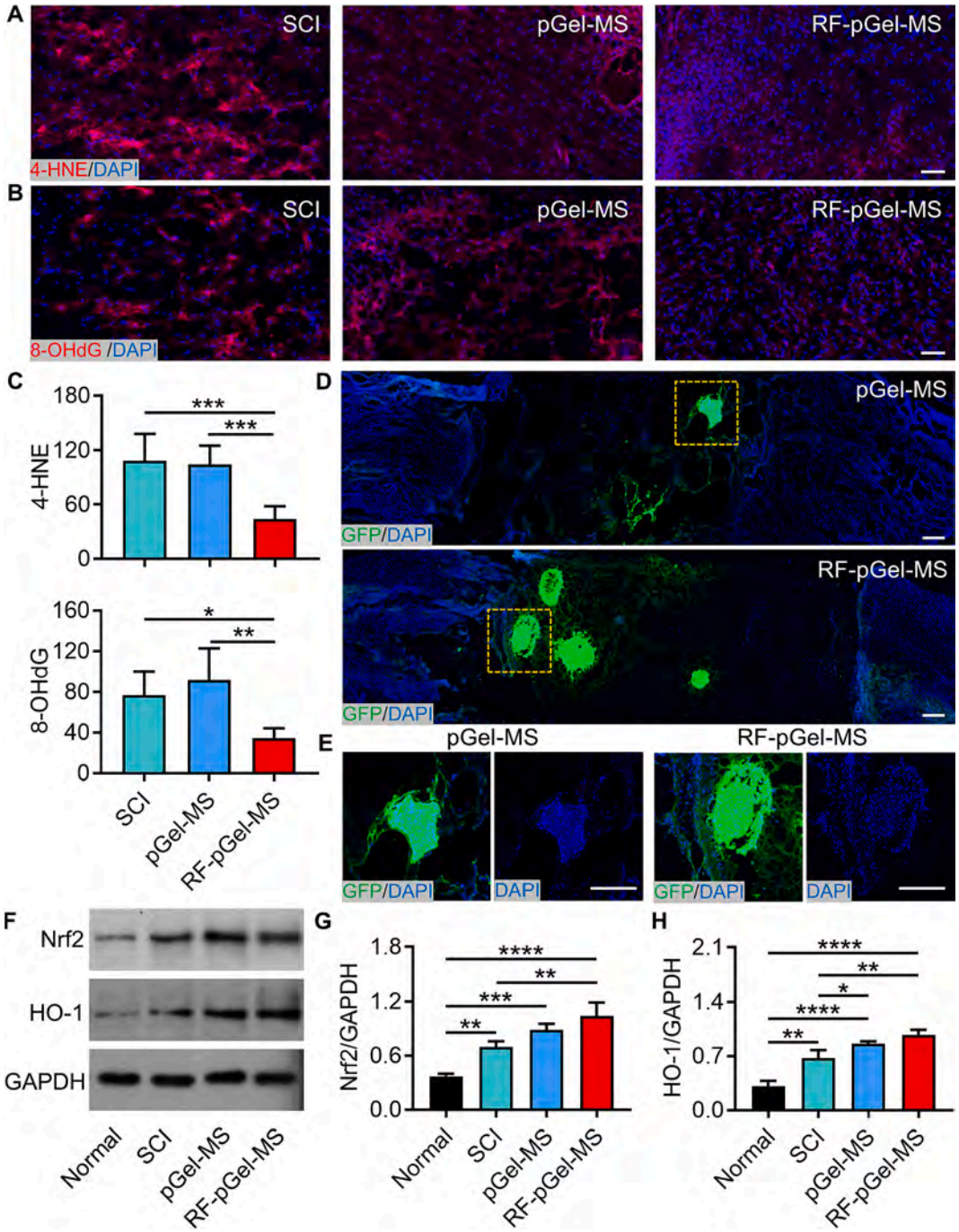

Fig. 5. Anti-peroxidative effect of RF-pGel-MS *in vivo* and mechanism investigation. (A-C) Immunofluorescent detection of 4-HNE (A) and 8-OHdG (B) expression levels in spinal cord lesions of SCI, pGel-MS, and RF-pGel-MS groups and their histogram of the fluorescence intensity (C, n = 3 × 2). Scale bar: 50 μm. (D) GFP-expressed MS distribution was detected in spinal cord tissues of pGel-MS, and RF-pGel-MS groups. Scale bar: 250 μm. (E) Represented detailed images of MS zoomed-in from yellow squares in (D). Scale bar: 250 μm. (F-H) Expression level of Nrf2 and HO-1 in spinal cord tissue detected by Western Blot (F) and the corresponding semi-quantitative analysis (G and H, n = 3). The data was shown as mean ± SD and analyzed by one-way ANOVA with multiple comparisons test. *P < 0.05, **P < 0.01, ***P < 0.001 and ****P < 0.0001. (For interpretation of the references to color in this figure legend, the reader is referred to the web version of this article.)

2.5. Promotion on functional recovery of RF-pGel-MS in the chronic phase

The therapeutic efficacy of pGel-MS or RF-pGel-MS was evaluated by implanting pGel-MS or RF-pGel-MS in fully transectioned SCI rats with a lesion gap (3 mm). Rats of non-treatment were performed as control. After surgery, rats exhibited total paralysis and urination dysfunction, indicating the successful establishment of SCI model. A slight decrease in body weight post-surgery was shown while no significance was found compared with normal rats, indicating the safety of scaffold implantation (Fig. 6A). Various degrees of locomotor and urination functions were gradually recovered and reached a plateau after 28 days (Fig. 6B). After 35-day treatment, the function restoration was achieved in pGel-MS and RF-pGel-MS group, with notable improvement on average BBB score (4.833 and 8.833, respectively).

Furthermore, the locomotor and electrophysiological recoveries were evaluated using Vicon system as depicted in Fig. 6C. The coordinates of labeled rat joints when free movement were recorded using

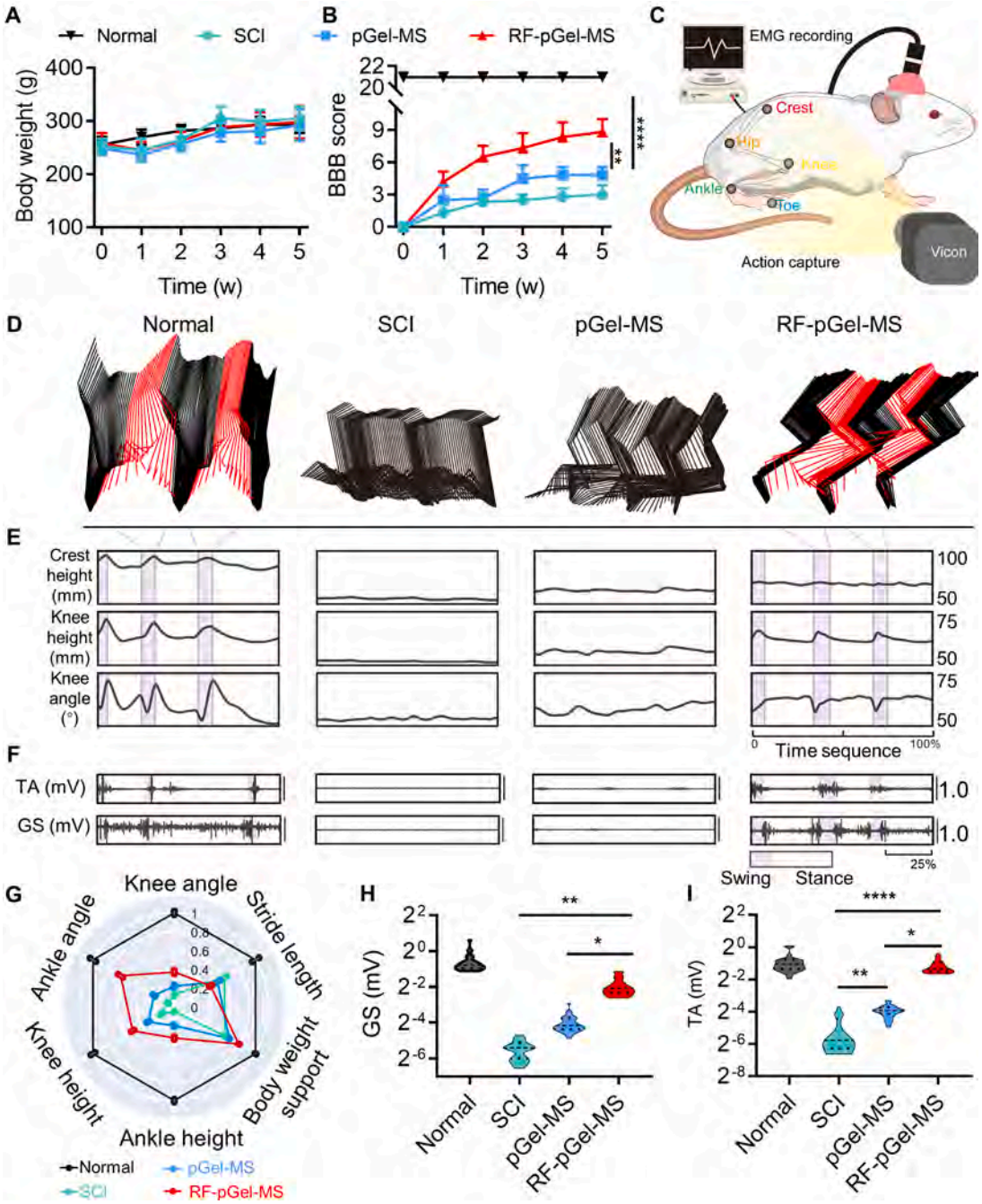

Fig. 6. The kinetics and the EMG recovery of rats after 35-day treatment. (A, B) Weekly body weights (A) and BBB scores (B) of rats in each group (n = 6). (C) Specific kinetics were recorded with five reflective balls attacked to hindlimb landmarks (crest, hip, knee, ankle, and toe) and tracked by the Vicon system. Besides, the EMG signals were recorded whilst the animals walking freely. (D) Representative trajectories of labeled joints were illustrated where the red color refers to the swing phase and the black means the stance or dragging. (E) Meanwhile, the relative kinetic traits were also shown, with pink intervals of swing phases. (F) And the typical EMG of TA and GS were also displayed. (G) The intergroup kinetic spectra were compared by the inverse-variance weighted mean of subgroup replication means, where one animal recorded by eight replicates (each took three consecutive steps). Body weight support (i.e., the crest height), the fluctuation height and the joint activity of two key articulates (knee and ankle), as well as the stride length, were illustrated in a radar map (n = 3). (H, I) The violin plots show the difference in the GS (H) and TA (I) signal intensity (n = 3 × 8). The data of (A and B) was shown as mean ± SD and analyzed by one-way ANOVA with multiple comparisons test. The data of (G-I) was shown as mean ± SEM and analyzed using the robust ANOVA with Tukey corrected posthoc test. *P < 0.05, **P < 0.01, ***P < 0.001 and ****P < 0.0001. (For interpretation of the references to color in this figure legend, the reader is referred to the web version of this article.)

Vicon system. The free-moving trajectory was obtained and analyzed based on the three consecutive steps of rats (Fig. 6D and S12). The black line in trajectory represented stance and dragging while red line meant swinging, respectively. Swinging behavior was found in rats of normal and RF-pGel-MS groups, indicating a hindlimb plantar placement or dorsal stepping (Vedio S2). Strikingly, the detailed analysis based on trajectory demonstrated substantial improvement in crest heights (body weight support), and the activity of knee (by the fluctuation range of heights and the oscillation range of knee angers) in RF-pGel-MS group (Fig. 6E, Fig. S13). The radar map also proved great recovery RF-pGel-MS in multiple indices including ankle height, ankle anger (Fig. 6G). These results suggested that RF-pGel-MS therapy remarkably promoted

the postinjury weight-bearing stepping ability.

The locomotor functional recovery could attribute to the electrophysiological recovery. The electromyogram (EMG) of hindlimb tibialis anterior muscle (TA) and extensor gastrocnemius soleus muscle (GS) were recorded during the free movement. Similarly, GS and TA showed higher EMG amplitudes in RF-pGel-MS while they were rarely active in SCI and pGel-MS groups (Fig. 6F, 6H and 6I). Despite the significant improvement, the rhythm of TA and GS was compromised in contrast to normal rats, which explained why they did not display a normal gait.

Neurofilament (NF), which represents a neuron, and glial fibrillary acidic protein (GFAP), which represents an active astrocyte, were used to identify the regeneration of nerve tissue following SCI. After devastating damage of SCI, almost no NF signal in spinal cord lesion was found in SCI group (Fig. S14). By contrast, implantation of pGel-MS facilitated the reconstruction of NF network as shown in both adjacent area and lesion area (Fig. 7A and 7B). Due to the dual regulation in the acute phase and chronic phase, NF fibers in RF-pGel-MS were dramatically increased especially in lesion area. A large number of nerve fibers were observed to distribute across the GFAP positive area to the lesion area (Fig. 7C-7F). Moreover, a longer average length of nerve fibers was observed in RF-pGel-MS compared with pGel-MS (Fig. 7G). In a word, the spinal cord in RF-pGel-MS had more and longer nerve fibers, which aided restoration of neural conduction. H&E staining sections of major organs indicated no severe side effects occurs after scaffolds

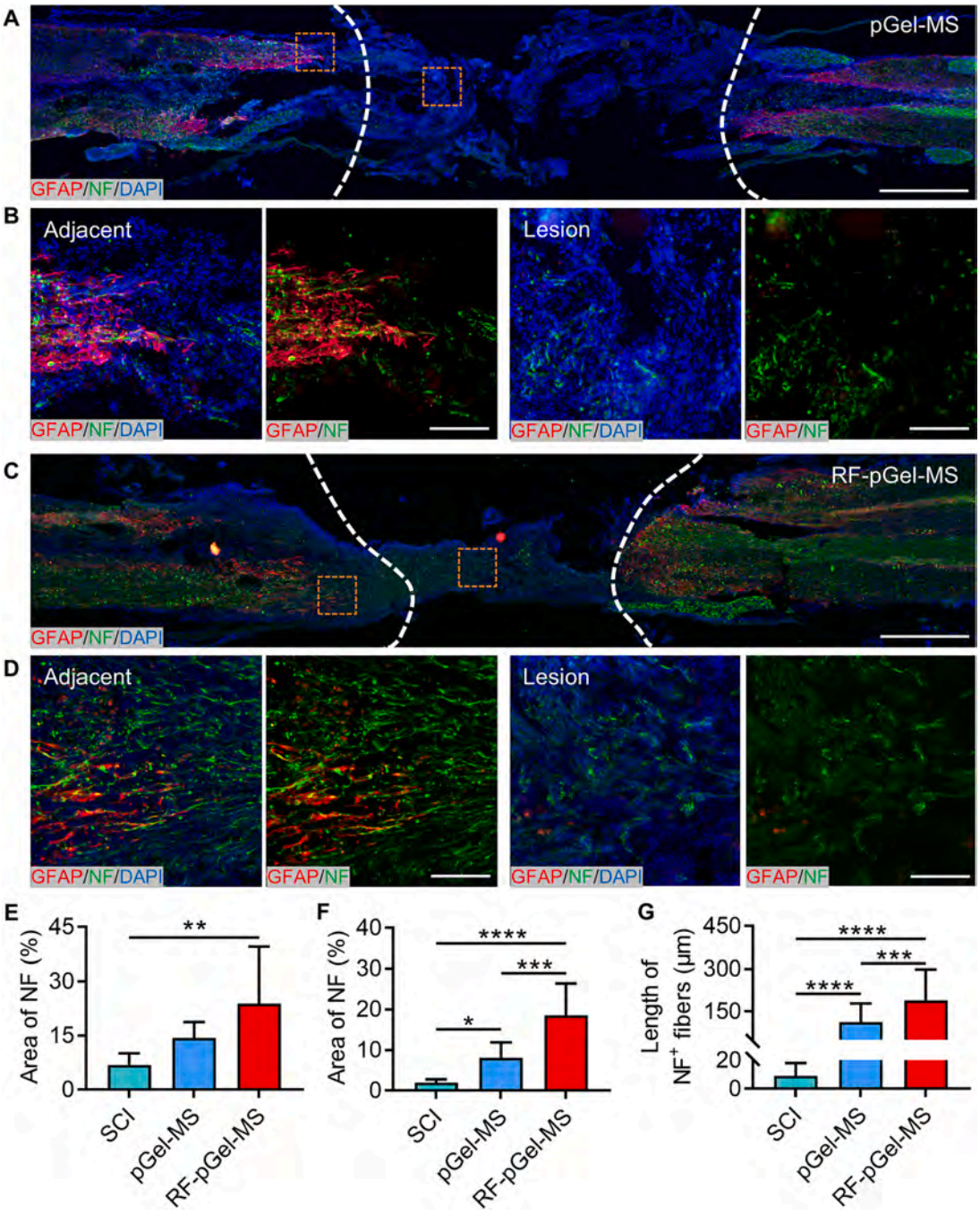

Fig. 7. Nerve regenerations in spinal cord tissue of rats after 35-day treatment. (A-D) Representative micrographs of NF and GFAP expressions and distributions in spinal cord tissues of rats in pGel-MS (A, B) and RF-pGel-MS (C, D) groups. Scale bar (A, C): 1 mm, scale bar (B, D): 100 μm. (E-G) Quantitative analysis of area percent of NF in adjacent (E, n = 3 × 3) and lesion (F, n = 3 × 3) and the length of NF^+ fibers in lesion area (G, n = 3 × 10) in each group. The data was shown as mean ± SD and analyzed by one-way ANOVA with multiple comparisons test. *P < 0.05, **P < 0.01, ***P < 0.001 and ****P < 0.0001.

implantation (Fig. S15). These results were consistent with locomotor and electrophysiological recovery, indicating the great synergistic efficacy of RF-pGel-MS.

3. Discussion

Owing to the limited potential of neural repair and regeneration in CNS, stem cell therapy has drawn more and more attention for its efficient capacity in regulating microenvironment and fostering neuron regeneration [16,17]. Among all types of stem cells, MSCs, which have a wide range of source and relatively higher safety, were extensively explored in tissue repair [18,19]. More than 300 clinical trials about MSCs therapy were completed as of 2020 [18]. Currently, there are two major obstacles to MSC treatment in SCI repair: (1) poor accumulation in lesions because of the rapid flow of cerebrospinal fluid or blood [20,21]; (2) low survival rate and poor cell viability due to the hostile environment (e.g. ROS) [22]. Consequently, we assumed that a scaffold system that could simultaneously localize and protect MSCs was promising. A scaffold with appropriate mechanical properties, biocompatibility, degradation, suitable morphology and tissue-mimic structure ensures a safe space for MSC and is supposed to promote the cell activities after implantation. Moreover, some anti-inflammation components can be co-loaded in scaffold to actively create favorable environment for MSC survival [23]. Hence, a RF coating scaffold (RF-pGel) fabricated using coating method was proposed in this study for MSC encapsulation and protection.

pGel is composed of gelatin, a natural ECM-derived material that has been widely proved its safety and biocompatibility in tissue engineering [24]. A porous and loose crosslinked network of pGel, was deemed to be suitable for cell growth and its mutual communications with the external environment. But the large pores of pGel make it difficult to effectively immobilized MSCs under the continuous flow of cerebrospinal fluid. To enhance the MSC adherence, some adhesive peptides or proteins were modified on scaffold. Our previous studies indicated that an adhesive peptide (Sequence: PPFLMLLKGSTR), which contained recognition site of αvβ3 integrin, was tethered on HA hydrogel. This peptide-tethered hydrogel was proved effective for MSC adhesion and spreading growth [25,26]. RGD tripeptide also can selectively binding to the ECM proteins like laminin and was widely used on hydrogel modification for MSC adherence [5,27]. While in this study, MSCs first spontaneously formed cell assemblies under the tight connection of integrin, cadherin. The cell assemblies then compressed with the rearrangement of actin fibers, formed mature MS [28]. MS with micron-size can be easily encapsulated and immobilized in pGel via steric hindrance and can maintain its spheroid structure for 7 d. The tentacle-like structure observed on MS further strengthened the MS adhesion on pGel. It eliminated the additional modification procedure and simplified the scaffold design. Moreover, the tightly-connected structure of MS overcame the rapid loss of MSCs in the local delivery method.

ROS generation is a key trigger of secondary injury [29], which causes more severe damage than the primary injury [3]. The resulted oxidative microenvironment prompts cellular apoptosis. Therefore, the rapid ROS scavenging in the acute phase is vital to inhibit the expansion of injury and maintain the vitality of implanted cells at early stage. H_2O_2 is one of the most prevalent reactive oxygen species (ROS) in tissue, which is mainly produced by spontaneous dismutation of precursor superoxide anion. H_2O_2 typically has a concentration between 1 and 8 μM, whereas activated macrophages and neutrophils in inflammatory disease may generate a higher local concentration in the range of 10 to 1000 μM [30]. To date, phenylboronic acid/ester is H_2O_2-sensitive and can be incorporated into the backbones of polymers to acquire H_2O_2-induced degradation of chains. In the current study, phenylboronic acid groups at both ends of TPA was first crosslinked with dihydroxy group of PVA to form RF. After implanting in inflammatory environment, H_2O_2-meidated oxidization leads to a rearrangement of benzene rings, resulting in H_2O_2 scavenging and the degradation of the whole structure of RF [31]. The high ROS sensitivity of phenylboronic acid group [32] enabled RF rapidly degrade H_2O_2 and effectively protect MS from peroxidation injury. *In vivo* study demonstrated that MS in RF-pGel-MS kept its spherical structure on day 4 post-injury. Furthermore, we discovered that pGel-MS upregulated Nrf2/HO-1 signaling pathway response to peroxidative damage in the acute phase, which has been reported previously [33,34]. And this promotion effect can be further enhanced under the protection of RF. However, it is noteworthy that the MS-mediated anti-peroxidative effect was limited as lipid and DNA peroxidation in pGel-MS group barely reduced contrast to SCI group. This suggested that the great anti-peroxidative efficacy mainly attributed to the outstanding ROS scavenging ability of RF and again explained why we construct RF for MS protection. Importantly, RF posed ROS-responsive degradation within 6 d as shown in *in vitro* study, which is consistent with period of the acute phase (0 ~ 72 h) [3]. As RF has a compact crosslink intensity and small pores, such degradation behavior would free up more space for MS living and nerve growth.

The initial purpose of MSC implantation for tissue repair was to replace the damaged cell, differentiate into desired cell types, and supply lost tissue [35]. However, with in-depth mechanism investigations, more and more studies contribute MSC efficacy to its paracrine effects [8], which release various types of trophic factors to mediate SCI repair [35]. And this paracrine effect can be further strengthened by 3D culture, which simulates *in vivo* conditions of MSCs. More cellular communications enabled expedited secretions of endogenous trophic factors. In our study, the trophic factors measurement by ELISA showed MS secreted a significantly higher levels of VEGF, GDNF, and NGF than MSC. Interestingly, MSs with different sizes or cell numbers were found a little difference in secretion behavior. MSs with relatively small size (MS2, MS3) showed more secreted level. PC12 cell differentiation test also indicated slightly better ability of MS2 and MS3 in promoting cell differentiation and neurite elongation. We speculated that the increase of MS size or cell number led to the difficulty of nutrient input and metabolite output, and ultimately influenced its paracrine ability [36]. Though the best size of MS was not further investigated, MS3 used in this study already exhibited outstanding secretion capacity and effective promotion on functional recovery in SCI rat model.

SCI is a complicated and knotty disease in CNS that manifests different features in the acute phase and chronic phase [29]. We assumed that the as-fabricated RF-pGel-MS can be utilized for dual-phase management of SCI via ROS scavenging in the acute phase and promotion of neural regeneration in the chronic phase. To test the efficacy of RF-pGel-MS, fully transectioned SCI model was built in rats. Despite SCI caused by transection is different with patients in clinic, it can minimize the efficacy of residual nerve bypass and maximize the efficacy of interventional on the damaged spinal cord [37]. After 35-day treatment, rats in RF-pGel-MS group showed much higher average BBB score, more weight-bearing support, stronger EMG signals and more nerve regenerations compared with SCI and pGel-MS groups, which proved great synergistic therapeutic effect of RF-pGel-MS and the importance of dual-phase regulation strategies in SCI repair. However, the gap in functional recovery between the rats in RF-pGel-MS and normal groups remained, suggesting the complete cure of SCI is still far away and needs more investigations in precision medicine.

4. Conclusion

This study constructed a composite scaffold system, RF-pGel-MS, which consisted of an outer RF, an inner pGel and encapsulated MSs, to realize dual-phase regulations in SCI repair. RF rapidly eliminated overproduced ROS to mitigate the expansion of secondary injury and protect the MS from peroxidative damage in the acute phase. MS with a 3D structure exhibited an enhanced paracrine effect and promoted neuronal regeneration in the chronic phase. The therapeutic efficacy of the proposed dual-phase treatment mediated by RF-pGel-MS was validated by the significantly promoted locomotor and electrophysiological

recovery in SCI rats. Overall, the current study provides a promising strategy with dual-phase regulation capacity for the synergistic treatment of SCI.

5. Materials and methods

5.1. Materials

Polyvinyl alcohol (PVA) was obtained from TCI chemicals (Shanghai, China), N,N,N',N'-Tetramethylmalonamide, 4-(Bromomethyl) phenylboronic acid were purchased from Macklin Inc. (Shanghai, China). Calcein AM, Propidium Iodide (PI), ROS assay kit were purchased from Beyotime Inc. (Shanghai, China). Agarose and H_2O_2 content assay kit were obtained from Solarbio Science & Technology Co., Ltd. (Beijing, China). CCK-8 kit was purchased from BOSTER Biological Technology Co., Ltd (Wuhan, China). NGF, GDNF and VEGF ELISA kits were bought from Multisciences Biotech, Co., Ltd. (Hangzhou, China). Porous GelMA and UV light were obtained from EFL technology (Suzhou, China). Human fibroblast growth factor-basic (FGF) and epidermal growth factor (EGF) were purchased from PeproTech, Inc. (Suzhou, China). GFP-encoded lentivirus and puromycin were obtained from Genechem Co., Ltd. (Shanghai, China). All chemicals obtained from the commercial source were used as received.

5.2. Cells and animals

PC12 cells obtained from iCell Bioscience Inc. (Shanghai, China) were cultured in RPMI 1640 medium supplied with 10% of fetal bovine serum (FBS), 5% of equine serum, 1% of penicillin (100 U/ml) and streptomycin (50 U/ml). Human umbilical cord-derived MSCs obtained from SinoCell Technology Co., Ltd. (Ningbo, China) were cultured in MEM-α medium supplied with 10% of fetal bovine serum (FBS), 10 μg of FGF and 10 μg of EGF. GFP-expressed MSCs were constructed by the transfection of MSCs using GFP-encoded lentivirus and puromycin was used to screen GFP-positive MSCs after transfection.

Female SD rats (220 ~ 250 g) were purchased from SLAC Laboratory Animal Co., Ltd. (Shanghai, China).

5.3. Synthesis of TPA and preparation of RF

TPA was synthesized following a previous study [2]. N,N,N',N'-tetramethylmalonamide (0.1 g), 4-(bromomethyl) phenylboronic acid (0.5 g) were dissolved in dimethyl formamide (DMF) and reacted at 60 °C for 24 h under continuous stirring. The mixture was poured into cold tetrahydrofuran (THF) to obtain TPA and washed with THF thrice. TPA was dissolved in DI water and dried under vacuum for purification and stored at room temperature. The chemical structure of TPA was confirmed using NMR spectroscope (AVANCE 500 M, Bruker Technology Co., Ltd.).

RF was fabricated by the mixture of PVA (50 mg/mL) and TPA (50 mg/mL) with equal volumes. RF was freezing dried and the microstructure was then detected by scanning electron microscope (Nova Nano 450, Thermo FEI).

To test ROS scavenging ability of RF, RF was added into H_2O_2 (1 mM) solution. The concentrations of H_2O_2 were measured at 0, 1, 2, 4, 8 and 16 h using H_2O_2 assay kit according to the protocol.

RF was immersed into PBS and H_2O_2 (1 mM) solution overnights and then oxygen generation was observed using a digital camera. The ROS-depended degradation was observed by taking photos of RF in PBS and H_2O_2 (1 mM) solution daily until complete degradation.

5.4. Construction and characterization of RF-pGel-MS

pGel was fabricated by UV crosslink (405 nm, 15 s) of porous GelMA solution (8%). PVA was casted into a strip sharp and then TPA was uniformly pipetted on the PVA to form RF. pGel was coated by RF to form RF-pGel. The morphology of pGel and RF-pGel was detected by stereo microscope (AZ100, Nikon corporation). The rheological tests of RF and pGel were conducted using rheometer (Mars40, ThermoFisher). The microstructure was scanned using scanning electron microscope and high-resolution miroCT (Skyscan1272, Bruker Technology Co., Ltd.). The 3D image of RF-pGel was reconstructed by Avizo software (Thermo Scientific). Volume fraction, pore area and pore volume were also calculated using Avizo software.

MS was constructed by 3D culture of MSCs. In brief, agarose solution (1%) was dropwise added into the 96-well plate (round bottom) to form a concave surface with low cellular adhesion. MSCs (cell number: 1.5×10^4) were dispensed in agarose-coated plate and gathered by centrifugation (1000 rpm) for 10 min. Finally, the mature MS was obtained after culture in a cell incubator for 3 days. The morphology of MS was observed by optical microscope (ECLIPSE Ti series, Nikon corporation) and scanning electron microscope.

MS was loaded in pGel by mixing with porous GelMA solution and crosslinked under the UV light. pGel-MS was cultured in MSC medium for 7 d and the morphology was observed using a fluorescence microscope (ECLIPSE Ti series, Nikon corporation). Then RF was coated around the pGel-MS to form RF-pGel-MS. MS distribution in RF-pGel-MS was detected by high-resolution miroCT.

5.5. Paracrine and neurotrophic effects of MS

MSs containing 6×10^4, 3×10^4 and 1.5×10^4 MSCs were fabricated as mentioned above to obtained MSs with different sizes (MS1, MS2, MS3). Then 3 MS1s, 6 MS2s, 12 MS3s and MSCs (total cell number: 1.8×10^5) were encapsulated in pGel and cultured in serum-free culture medium for 3 d. The culture medium was collected and secreted factors including NGF, GDNF and VEGF were measured using ELISA kits according to the protocols.

The neurotrophic effect of MS was further detected on PC12 cells. PC12 cells were cultured in 24-well plate overnights for cell attachment. pGel-MSC or pGel-MS (MS1, MS2, MS3) with same cell number were added and co-cultured for 3 d. pGel-MSC or pGel-MS were removed and PC12 cells were stained using calcein for 30 min. The morphology of cell was detected by confocal microscope (TCS SP8, Leica microsystems). The differentiation rate, average neurite number per cell and neurite length were analyzed using ImageJ software.

5.6. Anti-peroxidation study of RF in PC12 cells

The cytotoxicity of RF was detected in PC12 cells using CCK-8 method. RFs with various concentrations of TPA (50, 100, 200 mg/mL) were immersed in culture medium and incubated for 24 h. The RF-conditioned or normal culture medium was used to incubate PC12 cells (10^4 cells/well) for 24 h. After that, the culture medium was replaced by a fresh medium containing 10% of CCK-8 dye and incubate at 37 °C for 4 h. The OD value of each group was scanned at 450 nm by a microplate reader (Gen5, BioTek Instruments, Inc.). Then, the cytotoxicities of RF, pGel and RF-pGel to PC12 cells and MSCs were also tested.

The oxidative injury model was built in PC12 cells. RFs with various concentrations of TPA (0, 50, 100, 200 mg/mL) were incubated in culture medium containing H_2O_2 (1 mM) at room temperature for 24 h. 20 μL of incubated medium were added into PC12 cells to adjust H_2O_2 concentration to 200 μM. Fresh medium were added as control group. After the incubation for 24 h, the survival rate of PC12 was recorded using CCK-8 method. In another experiment, PC12 cells were cultured in medium containing H_2O_2 (500 μM) and incubated with RF (TPA: 50 mg/mL) for 24 h. ROS levels of PC12 cells with different treatments were detected by ROS probe, DCFH-AM. The average fluorescent intensity of cells was measured by flow cytometry (CytoFLEX LX, Beckman Life Sciences). The data were analyzed using FlowJo software.

5.7. Protection effect of RF-pGel for MS against ROS

pGel-MS and RF-pGel-MS were fabricated and culture in culture medium overnights. Then the culture medium was replaced by peroxidative medium containing H_2O_2 (500 μM). After incubation for 24 h, MSs were tested with live/dead assay according to the provided protocol. The samples were observed using confocal microscope.

In addition, the long-term protection effect was also investigated. MSs in pGel-MS and RF-pGel-MS were cultured in the medium as described above and H_2O_2 (500 μM) was added daily. The morphology of MS was observed daily by optical microscope.

5.8. Establishment of SCI rat and scaffold implantation

Female rats ranging from 220 ~ 250 g were anesthetized and hair removed. Laminectomy was conducted on T10 to expose spinal cord. The spinal cord was fully transected with a lesion gap (3 mm). After complete hemostasis, pGel-MS or RF-pGel-MS containing 1.8×10^5 MSCs were implanted into the lesions and surgical wound was successively sutured. Rats were received penicillin injection daily within first week and massage on bladder daily until bladder control returned. The *in vivo* degradation of RF-pGel-MS was detected by observing the morphology of spinal cord on day 7, 14, 21 and 28.

5.9. Behavioral and electrophysiological studies

Body weight and BBB score of rats were evaluated every week after surgery and hindlimb movement in an open field was recorded by digital camera (OsmoAction, Dj Innovations). On day 35, hindlimb joints of rats including crest, hip, knee, ankle and toe were labeled by anatomical landmarks. Then, the animals were walking freely and the landmarks were recorded to decipher the locomotor kinetics under the infrared 3D Motion System (Vicon Nexus, UK) according to a published article [38]. Typical traits and relative landmark trajectories were displayed, including the body weight support, the fluctuation range of height, and the oscillation range of joint angle. The swing and stance period were distinguished by whether or not away from the land of the labeled hindlimb. And the body weight support ability was defined by the height of the crest maker. The relative ability of kinetics traits was finally normalized and compared on a radar map.

For EMG signal recording, electrode implantation was performed blindly [39]. Briefly, 5 weeks post-injury animals were anesthetized and kept warm during the surgery. The ground lead was connected to a stainless-steel screw fixed on the skull. And the bipolar electrodes (AS632, Conner wire), tied on the header plate and went through subcutaneously, were inserted under the belly of TA and GS with a reference lead bonded to the ipsilateral tendon.

Seven days post-implantation, the interested hindlimb was labeled by five landmarks as above and wore a header lead which was connected up to an amplifier to detect the muscle strength. Next, the muscle activity when free-moving was recorded in the Neurostudio system (Braintech, China). Signals were filtered (band pass 20 Hz-1000 Hz) before computing the muscle amplitude.

Statistical analysis was performed on the R studio or the GraphPad. The Shapiro test and the Bartlett test were performed to verify the distribution and the homoscedasticity, separately. One-way or two-way ANOVA with inter-group comparison (Tukey corrected) was applied. Robust ANOVA was employed when the assumptions were violated [40]. All parameters were shown as the mean ± SEM and the significance was set when $P < 0.05$.

5.10. Tissue processing

To detect *in vivo* anti-peroxidative effect of RF-pGel-MS in acute phase, rats were sacrificed on day 4 and the spinal cord tissues were collected and sectioned into slices. The slices were stained using primary antibodies including 4-HNE antibody (Abcam, mouse, ab48506, 1:100), 8-OHdG antibody (Omni, mouse, OM176273, 1:50) and Alexa Fluor 594-conjugated secondary antibodies (Yeasen, donkey, 1:200). To investigate the MS distribution in in spinal cord, GFP-expressed MSCs were used to construct MSs and were observed by staining with GFP antibody (EarthOx, rabbit, E022200, 1:200) and Fluor 488-conjugated secondary antibodies (Yeasen, donkey, 1:200). Nrf2 and HO-1 expressions in spinal cord tissues were tested using corresponding antibodies (Nrf2: Abcam, rabbit, ab92946, 1:2000; HO-1: Abcam, rabbit, ab68477, 1:10000) by Western Blot test.

To test the tissue regeneration in chronic phase, rats were sacrificed and spinal cord and major organs were collected on day 35. For safety evaluation, heart, liver, spleen, lung and kidney were stained with hemotoxylin and eosin (H&E). For immunofluorescence analysis, spinal cords were sectioned into frozen slices. The slices were wash with PBS thrice following staining the primary antibodies including GFAP (BOSTER, rabbit, BA0056, 1:50), NF (CST, mouse, 2836, 1:200) at 4 °C overnights. Afterward, the slices were stained by fluorescent secondary antibodies at 37 °C for 1 h. Mounting medium containing DAPI was dropwise added to label nuclei. The fluorescent images of slices were scanned by Slide Scanner (VS200, Olympus Corporation).

5.11. Statistical analysis

The data were presented as mean ± SD or mean ± SEM and analyzed using GraphPad Prism software with Student's *t*-test between two groups or one-way ANOVA among multiple groups. Significance was set when $P < 0.05$.

Data availability

All data that support the findings of this study are available from the corresponding author upon reasonable request.

Author Contributions

J. C. and J. G. conceived the idea and designed the experiment. S. F. discussed the experimental design. J. C., J. W., J. M. and L. L. conducted experiments and data analysis and wrote the manuscript. X. Z., T. H.and T. M. assisted with the cell experiments. M. Z. and X. D. assisted with the animal experiments. X. W. provided methodology support. S. F. and J. G. helped with the manuscript writing and revision. J.C. and J. W. contributed equally to this work.

Declaration of Competing Interest

The authors declare that they have no known competing financial interests or personal relationships that could have appeared to influence the work reported in this paper.

Data availability

Data will be made available on request.

Acknowledgments

This study was supported by the National Key Research and Development Project of Stem Cell and Transformation Research (grant numbers: 2019YFA0112100, 2019YFA0112102) and National Natural Science Foundation of China (grant numbers: 81973252, 81620108028, 81971866). We thank for the technical support from core facility platform of Zhejiang University School of Medicine. We thank Dandan Song in the Center of Cryo-Electron Microscopy(CCEM), Zhejiang University for her technical assistance on Scanning Electron Microscopy.

Appendix A. Supplementary data

Supplementary data to this article can be found online at https://doi.org/10.1016/j.cej.2023.142192.

References

[1] G. Courtine, M.V. Sofroniew, Spinal cord repair: advances in biology and technology, Nat. Med. 25 (6) (2019) 898–908, https://doi.org/10.1038/s41591-019-0475-6.

[2] H. Zhao, J. Huang, Y. Li, X. Lv, H. Zhou, H. Wang, Y. Xu, C. Wang, J. Wang, Z. Liu, ROS-scavenging hydrogel to promote healing of bacteria infected diabetic wounds, Biomaterials 258 (2020), 120286, https://doi.org/10.1016/j.biomaterials.2020.120286.

[3] C.S. Ahuja, J.R. Wilson, S. Nori, M.R.N. Kotter, C. Druschel, A. Curt, M.G. Fehlings, Traumatic spinal cord injury, Nat. Rev. Dis. Primers. 3 (2017) 17018, https://doi.org/10.1038/nrdp.2017.18.

[4] J. Koffler, W. Zhu, X. Qu, O. Platoshyn, J.N. Dulin, J. Brock, L. Graham, P. Lu, J. Sakamoto, M. Marsala, S. Chen, M.H. Tuszynski, Biomimetic 3D-printed scaffolds for spinal cord injury repair, Nat. Med. 25 (2) (2019) 263–269, https://doi.org/10.1038/s41591-018-0296-z.

[5] S. Papa, I. Vismara, A. Mariani, M. Barilani, S. Rimondo, M. De Paola, N. Panini, E. Erba, E. Mauri, F. Rossi, G. Forloni, L. Lazzari, P. Veglianese, Mesenchymal stem cells encapsulated into biomimetic hydrogel scaffold gradually release CCL2 chemokine in situ preserving cytoarchitecture and promoting functional recovery in spinal cord injury, J. Control. Release 278 (2018) 49–56, https://doi.org/10.1016/j.jconrel.2018.03.034.

[6] A. Higuchi, S.S. Kumar, G. Benelli, Q. Ling, H. Li, A. Alarfaj, M.A. Munusamy, T. Sung, Y. Chang, K. Murugan, Biomaterials used in stem cell therapy for spinal cord injury, Prog. Mater. Sci. 103 (2019) 374–424, https://doi.org/10.1016/j.pmatsci.2019.02.002.

[7] J. Redondo, P. Sarkar, K. Kemp, K.J. Heesom, A. Wilkins, N.J. Scolding, C.M. Rice, Dysregulation of mesenchymal stromal cell antioxidant responses in progressive multiple sclerosis, Stem Cell. Transl. Med. 7 (10) (2018) 748–758, https://doi.org/10.1002/sctm.18-0045.

[8] X. Fan, Y. Zhang, X. Li, Q. Fu, Mechanisms underlying the protective effects of mesenchymal stem cell-based therapy, Cell. Mol. Life Sci. 77 (14) (2020) 2771–2794, https://doi.org/10.1007/s00018-020-03454-6.

[9] S. Joshi-Barr, L.G. de Caroline, E. Mahmoud, A. Almutairi, Exploiting oxidative microenvironments in the body as triggers for drug delivery systems, Antioxid. Redox Sign. 21 (5) (2014) 730–754, https://doi.org/10.1089/ars.2013.5754.

[10] B. Yang, Y. Chen, J. Shi, Reactive oxygen species (ROS)-based nanomedicine, Chem. Rev. 119 (8) (2019) 4881–4985, https://doi.org/10.1021/acs.chemrev.8b00626.

[11] Y. Yao, H. Zhang, Z. Wang, J. Ding, S. Wang, B. Huang, S. Ke, C. Gao, Reactive oxygen species (ROS)-responsive biomaterials mediate tissue microenvironments and tissue regeneration, J. Mater. Chem. B 7 (33) (2019) 5019–5037, https://doi.org/10.1039/C9TB00847K.

[12] N. Yang, W. Xiao, X. Song, W. Wang, X. Dong, Recent advances in tumor microenvironment hydrogen peroxide-responsive materials for cancer photodynamic therapy, Nano-micro Lett. 12 (1) (2020) 15, https://doi.org/10.1007/s40820-019-0347-0.

[13] L. Fan, C. Liu, X. Chen, Y. Zou, Z. Zhou, C. Lin, G. Tan, L. Zhou, C. Ning, Q. Wang, Directing induced pluripotent stem cell derived neural stem cell fate with a three-dimensional biomimetic hydrogel for spinal cord injury repair, ACS Appl. Mater. Inter. 10 (21) (2018) 17742–17755, https://doi.org/10.1021/acsami.8b05293.

[14] Y. Jiang, P. Fu, Y. Liu, C. Wang, P. Zhao, X. Chu, X. Jiang, W. Yang, Y. Wu, Y. Wang, G. Xu, J. Hu, W. Bu, Near-infrared light-triggered NO release for spinal cord injury repair, Sci. Adv. 6 (39) (2020) 3513, https://doi.org/10.1126/sciadv.abc3513.

[15] R.G. Bardallo, A. Panisello-Rosello, S. Sanchez-Nuno, N. Alva, J. Rosello-Catafau, T. Carbonell, Nrf2 and oxidative stress in liver ischemia/reperfusion injury, FEBS J. 464 (17) (2021) 1742, https://doi.org/10.1111/febs.16336.

[16] J. Cao, J. Wu, J. Mu, S. Feng, J. Gao, The design criteria and therapeutic strategy of functional scaffolds for spinal cord injury repair, Biomat. Sci. 9 (13) (2021) 4591–4606, https://doi.org/10.1039/D1BM00361E.

[17] T.H. Hutson, S. Di Giovanni, The translational landscape in spinal cord injury: focus on neuroplasticity and regeneration, Nat. Rev. Neurol. 15 (12) (2019) 732–745, https://doi.org/10.1038/s41582-019-0280-3.

[18] O. Levy, R. Kuai, E.M.J. Siren, D. Bhere, Y. Milton, N. Nissar, M. De Biasio, M. Heinelt, B. Reeve, R. Abdi, M. Alturki, M. Fallatah, A. Almalik, A.H. Alhasan, K. Shah, J.M. Karp, Shattering barriers toward clinically meaningful MSC therapies, Sci. Adv. 6 (30) (2020) eaba6884, https://doi.org/10.1126/sciadv.aba6884.

[19] A. Andrzejewska, S. Dabrowska, B. Lukomska, M. Janowski, Mesenchymal stem cells for neurological disorders, Adv. Sci. 8 (7) (2021) 27, https://doi.org/10.1002/advs.202002944.

[20] C.M. Madl, S.C. Heilshorn, H.M. Blau, Bioengineering strategies to accelerate stem cell therapeutics, Nature 557 (7705) (2018) 335–342, https://doi.org/10.1038/s41586-018-0089-z.

[21] J.A. Burdick, R.L. Mauck, S. Gerecht, To serve and protect: hydrogels to improve stem cell-based therapies, Cell Stem Cell 18 (1) (2016) 13–15, https://doi.org/10.1016/j.stem.2015.12.004.

[22] T. Führmann, R.Y. Tam, B. Ballarin, B. Coles, I.E. Donaghue, D. van der Kooy, A. Nagy, C.H. Tator, C.M. Morshead, M.S. Shoichet, Injectable hydrogel promotes early survival of induced pluripotent stem cell-derived oligodendrocytes and attenuates longterm teratoma formation in a spinal cord injury model, Biomaterials 83 (2016) 23–36, https://doi.org/10.1016/j.biomaterials.2015.12.032.

[23] Q. Zhang, B. Shi, J. Ding, L. Yan, J.P. Thawani, C. Fu, X. Chen, Polymer scaffolds facilitate spinal cord injury repair, Acta Biomater. 88 (2019) 57–77, https://doi.org/10.1016/j.actbio.2019.01.056.

[24] A.G. Kurian, R.K. Singh, K.D. Patel, J.H. Lee, H.W. Kim, Multifunctional GelMA platforms with nanomaterials for advanced tissue therapeutics, Bioact. Mater. 8 (2022) 267–295, https://doi.org/10.1016/j.bioactmat.2021.06.027.

[25] L. Li, M. Han, X. Jiang, X. Yin, F. Chen, T. Zhang, H. Ren, J. Zhang, T. Hou, Z. Chen, H. Ou-Yang, Y. Tabata, Y. Shen, J. Gao, Peptide-tethered hydrogel scaffold promotes recovery from spinal cord transection via synergism with mesenchymal stem cells, ACS Appl. Mater. Interfaces 9 (4) (2017) 3330–3342, https://doi.org/10.1021/acsami.6b12829.

[26] L. Li, B. Xiao, J. Mu, Y. Zhang, C. Zhang, H. Cao, R. Chen, H.K. Patra, B. Yang, S. Feng, Y. Tabata, N.K.H. Slater, J. Tang, Y. Shen, J. Gao, A MnO_2 nanoparticle-dotted hydrogel promotes spinal cord repair via regulating reactive oxygen species microenvironment and synergizing with mesenchymal stem cells, ACS Nano 13 (12) (2019) 14283–14293, https://doi.org/10.1021/acsnano.9b07598.

[27] I. Caron, F. Rossi, S. Papa, R. Aloe, M. Sculco, E. Mauri, A. Sacchetti, E. Erba, N. Panini, V. Parazzi, M. Barilani, G. Forloni, G. Perale, L. Lazzari, P. Veglianese, A new three dimensional biomimetic hydrogel to deliver factors secreted by human mesenchymal stem cells in spinal cord injury, Biomaterials 75 (2016) 135–147, https://doi.org/10.1016/j.biomaterials.2015.10.024.

[28] W. Kim, Y. Gwon, S. Park, H. Kim, J. Kim, Therapeutic strategies of three-dimensional stem cell spheroids and organoids for tissue repair and regeneration, Bioact. Mater. 19 (2023) 50–74, https://doi.org/10.1016/j.bioactmat.2022.03.039.

[29] G. David, S. Mohammadi, A.R. Martin, J. Cohen-Adad, N. Weiskopf, A. Thompson, P. Freund, Traumatic and nontraumatic spinal cord injury: pathological insights from neuroimaging, Nat. Rev. Neurol. 15 (12) (2019) 718–731, https://doi.org/10.1038/s41582-019-0270-5.

[30] J.R. Burgoyne, S. Oka, N. Ale-Agha, P. Eaton, Hydrogen peroxide sensing and signaling by protein kinases in the cardiovascular system, Antioxid. Redox Signal 18 (9) (2013) 1042–1052, https://doi.org/10.1089/ars.2012.4817.

[31] J. Wang, Y. Zhang, E. Archibong, F.S. Ligler, Z. Gu, Leveraging H_2O_2 levels for biomedical applications, Adv. Biosyst. 1 (9) (2017) e1700084.

[32] J. Ding, Y. Yao, J. Li, Y. Duan, J.R. Nakkala, X. Feng, W. Cao, Y. Wang, L. Hong, L. Shen, Z. Mao, Y. Zhu, C. Gao, A reactive oxygen species scavenging and O_2 generating injectable hydrogel for myocardial infarction treatment in vivo, Small 16 (48) (2020) 2005038, https://doi.org/10.1002/smll.202005038.

[33] J. Li, D. Li, X. Liu, S. Tang, F. Wei, Human umbilical cord mesenchymal stem cells reduce systemic inflammation and attenuate LPS-induced acute lung injury in rats, J. Inflamm. 9 (1) (2012) 33, https://doi.org/10.1186/1476-9255-9-33.

[34] Z. Zhang, W. Zhu, H. Ren, X. Zhao, S. Wang, H. Ma, X. Shi, Mesenchymal stem cells increase expression of heme oxygenase-1 leading to anti-inflammatory activity in treatment of acute liver failure, Stem Cell Res. Ther. 8 (1) (2017) 70, https://doi.org/10.1186/s13287-017-0524-3.

[35] V. Veneruso, F. Rossi, A. Villella, A. Bena, G. Forloni, P. Veglianese, Stem cell paracrine effect and delivery strategies for spinal cord injury regeneration, J. Control. Release 300 (2019) 141–153, https://doi.org/10.1016/j.jconrel.2019.02.038.

[36] M.C. Decarli, R. Amaral, D.P.D. Santos, L.B. Tofani, E. Katayama, R.A. Rezende, J. V.L.d. Silva, K. Swiech, C.A.T. Suazo, C. Mota, L. Moroni, A.M. Moraes, Cell spheroids as a versatile research platform: formation mechanisms, high throughput production, characterization and applications, Biofabrication 13 (3) (2021) 032002, https://doi.org/10.1088/1758-5090/abe6f2.

[37] B. Fan, Z. Wei, S. Feng, Progression in translational research on spinal cord injury based on microenvironment imbalance, Bone Res. 10 (1) (2022) 35, https://doi.org/10.1038/s41413-022-00199-9.

[38] J. Ye, S. Jin, W. Cai, X. Chen, H. Zheng, T. Zhang, W. Lu, X. Li, C. Liang, Q. Chen, Y. Wang, X. Gu, B. Yu, Z. Chen, X. Wang, Rationally designed, self-assembling, multifunctional hydrogel depot repairs severe spinal cord injury, Adv. Healthc. Mater. 10 (13) (2021) e2100242, https://doi.org/10.1002/adhm.202100242.

[39] B. Chen, Y. Li, B. Yu, Z. Zhang, B. Brommer, P.R. Williams, Y. Liu, S.V. Hegarty, S. Zhou, J. Zhu, H. Guo, Y. Lu, Y. Zhang, X. Gu, Z. He, Reactivation of dormant relay pathways in injured spinal cord by KCC2 manipulations, Cell 174 (3) (2018) 521–535.e13, https://doi.org/10.1016/j.cell.2018.08.050.

[40] M. Koller, Robustlmm: an R package for robust estimation of linear mixed-effects models, J. of Stat. Softw. 75 (6) (2016) 1–24, https://doi.org/10.18637/jss.v075.i06.